



# Carbide Dissolution/Carbon Loss as a Function of Spray Distance in Unshrouded/Shrouded Plasma Sprayed $\text{Cr}_3\text{C}_2\text{-NiCr}$ Coatings

S. Matthews

(Submitted July 22, 2014; in revised form October 23, 2014)

Thermal spraying of  $\text{Cr}_3\text{C}_2\text{-NiCr}$  composites generates varying degrees of carbide dissolution into the Ni binder. During high-temperature exposure, the carbide dissolution zones precipitate high concentrations of small carbides which develop into finely structured networks. This raises the possibility of producing unique tailored carbide composite structures through the generation of controlled carbide dissolution and appropriate heat treatment. The first step in this process is to produce a supersaturated Ni-Cr-C solid solution from which the carbide phase could be precipitated. In a previous work, a broad range of plasma parameters were trialed to assess their effect on the degree of carbide dissolution at a fixed spray distance of 100 mm. The current two-part work builds on the most promising plasma parameters from those trials. In Part 1 of this two-part article series, the effect of spray distance on the extent of carbide dissolution and carbon loss during high energy plasma spraying was investigated. The effectiveness of solid shield and gas shrouding is contrasted, and the mechanisms by which they influence the degree of decarburization discussed.

**Keywords** carbide dissolution,  $\text{Cr}_3\text{C}_2\text{-NiCr}$ , decarburization, gas shrouding, shrouded plasma spray, spray distance

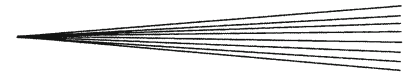
## 1. Introduction

$\text{Cr}_3\text{C}_2\text{-NiCr}$  thermal spray coatings are widely used to mitigate wear and corrosion at elevated temperatures where more wear resistant WC-Co cermets cannot be used due to their poor oxidation performance (Ref 1-3). It has been shown across several studies that thermally sprayed carbide composite coatings that retain a high carbide content and undergo minimal carbide degradation in-flight, typically show superior wear resistance (Ref 3-6). Therefore, it has become a conventional practice in the production of carbide composite coatings to optimize the deposition parameters to melt the metallic binder, in order to achieve high deposit efficiency, while at the same time keeping the particle temperature low and the in-flight time short to minimize carbide dissolution and decarburisation. For these reasons, HVOF spraying has become the industry standard for producing carbide composite thermal spray coatings.

During heat treatment of HVOF sprayed  $\text{Cr}_3\text{C}_2\text{-NiCr}$  coatings, it has been observed that zones of high carbide dissolution precipitate high concentrations of small carbide grains which quickly develop into finely structured and interconnected carbide networks (Ref 5-8). The significant variation in carbide structures developed as a function of carbide dissolution and subsequent heat treatment raises the possibility of tailoring the carbide phase morphology to exploit the beneficial wear resistance of submicron carbide grains or the development of other unique composite structure functionalities.

The first step in exploring this concept for  $\text{Cr}_3\text{C}_2\text{-NiCr}$  composite coatings is the production of a supersaturated solid solution of Ni-Cr-C from which high concentrations of carbides could be precipitated with suitable heat treatment. In a marked deviation from convention, the approach taken in this project was to spray a conventional  $\text{Cr}_3\text{C}_2\text{-NiCr}$  agglomerated and sintered powder under high-power plasma conditions. A high-energy, high-temperature plasma was used, rather than HVOF spraying, in order to generate as much carbide dissolution as possible to produce the greatest amount of supersaturated Ni-Cr-C material in the coating. In the lead-up to the current work, a broad range of plasma conditions (variations in nozzle geometry, Ar-He and Ar- $\text{H}_2$  plasma compositions, gas flow rate, and current), with and without shrouding, were investigated at a spray distance of 100 mm to assess their effect on the extent of carbide dissolution and carbon loss (Ref 9). A key outcome from that work was that shrouding had a significant effect on the extent of carbide dissolution, oxide formation, carbon loss, and the deposit

S. Matthews, School of Engineering and Advanced Technology, Massey University, Private Bag 102904, Auckland 0745, New Zealand. Contact e-mail: s.matthews@massey.ac.nz.

**Table 1 Plasma spray parameters**

Trial number/ description	Nozzle type	Shroud	Spray distance, mm	Ar flow, SLPM	Secondary gas	Secondary flow, SLPM	Carrier gas, SLPM	Current, A	Power, kW
CD01 Ar-H <sub>2</sub> low flow	Mach II	No	100, 120	50	H <sub>2</sub>	5	2	600	30
CD02 Ar-H <sub>2</sub> high flow	Mach II	No	100, 120	85	H <sub>2</sub>	7	3	800	56
CD03 Ar-H <sub>2</sub> low flow	Mach II	Yes (Solid Shroud)	100, 120	50	H <sub>2</sub>	5	2	600	30
CD04 Ar-H <sub>2</sub> high flow	Mach II	Yes (Solid Shroud)	100, 120	85	H <sub>2</sub>	7	3	800	56
CD05 Ar-He	Subsonic	No	80, 100, 120	40	He	9	2.5	700	37.8
CD06 Ar-H <sub>2</sub>	Subsonic	No	80, 100, 120	49	H <sub>2</sub>	5	2	600	33
CD07 Ar-He	Subsonic	Yes (Gas Shroud)	80, 100, 120	40	He	9	2.5	700	37.8
CD08 Ar-H <sub>2</sub>	Subsonic	Yes (Gas Shroud)	80, 100, 120	49	H <sub>2</sub>	5	2	600	33

efficiency of the Cr<sub>3</sub>C<sub>2</sub>-NiCr coatings. The current work builds on these preliminary trials by analyzing in detail the effect of spray distance on the coating attributes sprayed under the most promising plasma parameter settings. In part 1 of this two-part article series the effect of spray distance on the extent of carbide dissolution and carbon loss during high energy spraying of Cr<sub>3</sub>C<sub>2</sub>-NiCr coatings is presented. The effectiveness of solid shield shrouding and gas shrouding is discussed in relation to the minimization of decarburisation. The second part of this article series analyzes the effect of spray distance on the compositional development in these coatings (Ref 10).

## 2. Experimental Procedure

An agglomerated and sintered Cr<sub>3</sub>C<sub>2</sub>-NiCr powder (Amperit 588 (H.C.Starck, Munich, Germany)) (nominal size  $-45/+15 \mu\text{m}$ ) was sprayed onto degreased and grit-blasted mild steel substrates (100 mm × 25 mm × 3 mm) using a Praxair SG-100 plasma torch (Praxair Surface Technologies, Indianapolis, USA). The torch was mounted on a 6 axis robot which sprayed the samples in a horizontal raster pattern from the top to the bottom. Ten passes were applied for each plasma parameter setting. The substrates were mounted to a stepped spray stand that enabled coatings to be sprayed at 80, 100, and 120 mm at the same time. The coatings in this work that were sprayed at 80 and 120 mm were sprayed at the same time as the 100 mm spray distance samples that were analyzed in Ref 9. The results from the analysis of the 100 mm spray distance samples reported in Ref 9 have been summarized in this work in order to contrast the effect of the spray distance on the coating response.

Two plasma set-ups were used—a high-velocity plasma set-up using a “Mach II” anode nozzle, and a lower velocity plasma set-up using a “Subsonic” anode nozzle—both with single internal “forward” injection powder injectors. The trade names “Subsonic” and “Mach II” differentiate the two different anode nozzle geometries and are not directly related to the actual velocities generated in each nozzle. The parameter settings used for each plasma set-up are presented in Table 1. These were the two most promising parameter settings for each plasma set-up from the preliminary trials in Ref 9 based on the degree of carbide dissolution and coating quality. The

plasma parameters were well outside those recommended for this plasma torch. They resulted in extremely rapid wear of the electrodes that required replacement after only a few short spray trials. These settings were used to generate high-energy conditions to achieve high degrees of carbide dissolution, but were not recommended for standard spraying. For each plasma set-up, all of the trials were sprayed in air (unshrouded trials) and then repeated using shrouding. The unshrouded trials were used to visually optimize the carrier gas flow to achieve powder trajectories with low deviations from the plasma centreline at a distance of 100 mm. This was critical in order to avoid particles passing through the plasma and impacting on the inner wall of the shroud or the gas shroud, in the subsequent shrouded trials (Ref 11). In the Mach II anode nozzle trials, the tungsten insert was removed from the power injector to increase the internal diameter and provide greater flexibility in adjusting the carrier gas flow rate.

The Mach II anode nozzle shrouded trials were sprayed with a 90-mm-long solid conical coaxial copper shroud, Fig. 1(a). The specifics of the shroud design and its operation have been described in detail in Ref 12. Argon gas was injected internally through holes in the shroud wall at 3SLPM. An external coaxial argon gas shroud was formed via a circular slot from the front of the shroud using an argon gas flow of 300SLPM. Because the shroud was 90-mm long, samples were only sprayed at 100 and 120 mm spray distances.

The subsonic anode nozzle shrouded trials used a shorter shroud segment to form a protective gas shroud, rather than using the solid shroud for reasons discussed in Ref 9. The 25 mm front section of the solid shroud was removed and bolted directly to the plasma torch via an interface plate. Argon was fed to this shroud segment at 300SLPM to form a 40 mm diameter coaxial gas shroud, Fig. 1(b). This provided physical protection from air entrainment over the first 25 mm but relied on the gas shroud to prevent air ingress at longer distances. Samples were sprayed at distances of 80, 100 and 120 mm.

Coating samples cut from the sprayed substrates were mounted in cross section under vacuum in epoxy and metallographically prepared to a final 1  $\mu\text{m}$  diamond polish. Scanning electron microscopy (SEM) (FEI Quanta F, USA)(FEI, Oregon, USA) was used to analyze the samples using back-scattered electron imaging (BSE). Images were analyzed [software package ImageJ (Ref 13)]

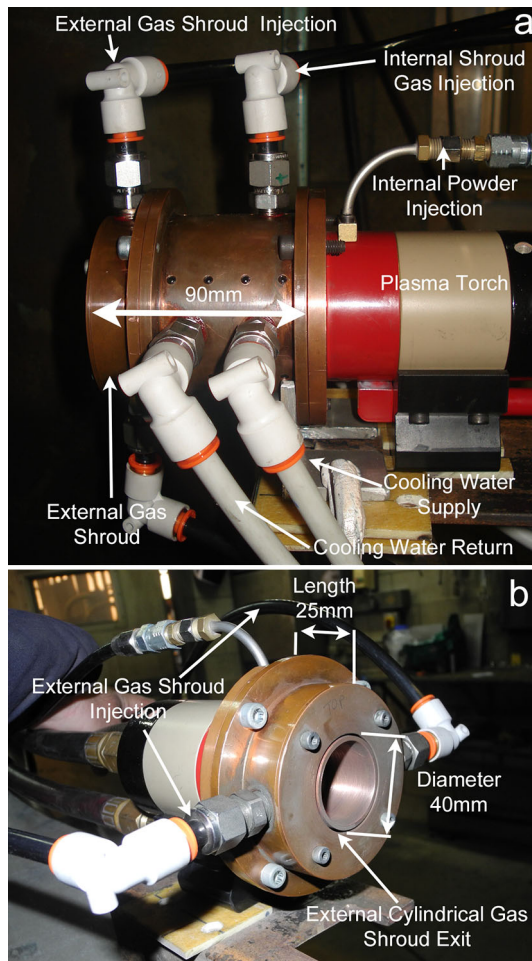


**Fig. 1** Images of the solid conical coaxial copper shroud used in the Mach II nozzle trials (a) and the shorter shroud segment used to form the coaxial gas shroud in the subsonic nozzle trials (b)

to quantify the coating thickness (magnification  $500\times$ ), the combined “porosity+oxide” content (magnification  $2000\times$ ) and the retained carbide content (defined as the total carbide volume fraction of the coating, excluding the porosity and oxide content)(magnification  $2000\times$ ) on at least five images per sample. Energy dispersive x-ray spectroscopy (EDS)(EDAX, New Jersey, USA) was used to measure the bulk normalized Cr and Ni concentrations on full frame images at  $2000\times$ . X-ray diffraction (XRD)(D2 Phaser (Bruker AXS GmbH, Karlsruhe, Germany))(Cu source at 30 kV and 10 mA,  $2\theta=20-80^\circ, 0.02^\circ/\text{step}, 0.8 \text{ s}/\text{step}$ ) was used to characterize the coating composition. The surface of the coating samples was first ground and polished to a  $3 \mu\text{m}$  diamond polish finish to remove any surface oxides and reduce the surface roughness. Phase identification was performed using the Bruker EVA software.

The reduction in carbon content between the starting powder and the plasma sprayed coatings was calculated using the method detailed in Ref 9. This method was adopted due to there being insufficient coating material for a conventional LECO combustion carbon analysis.

Coating samples were heat treated in air at  $800^\circ\text{C}$  for 3 h to enable the metastable and amorphous phases in the as-sprayed coatings to tend toward equilibrium (Ref 5, 6, 8). The samples were ground and polished to a  $3 \mu\text{m}$  diamond polish finish to remove the oxidized material at the surface prior to analysis. Rietveld fitting of the XRD pattern using the MAUD software package (Ref 14) was used to quantify the concentration of the coating phases, from which the elemental composition of the coating was calculated. The Cr content of the Ni alloy was determined from the alloy unit cell dimensions using the correlation in Ref 15. It was assumed that the carbon content of the Ni alloy was negligible and that the carbide compounds  $\text{Cr}_3\text{C}_2$  and  $\text{Cr}_7\text{C}_3$  contained negligible concentrations of Ni.  $\text{Cr}_2\text{O}_3$  was the only oxide formed and its concentration was quantified for the purposes of determining the elemental Cr concentration. It was assumed that no carbon was lost from the samples due to oxidation during heat treatment.

The “indicative carbon loss” was calculated by taking the difference in the carbon weight percent values between the powder and the coating, and dividing this by the original carbon weight percent composition in the powder. This calculation does not take into account that the mass of the coating produced from a given quantity of powder will be less than that of the starting powder due to carbon loss. Attempts were made to correct this by using the Ni weight percent as an internal standard, on the assumption that no Ni was lost during spraying. In this way, a corrected value for the true mass of carbon in each coating could be determined, from which the actual carbon loss during spraying could then be calculated. However, small variations in the Ni weight percent content calculated from the Rietveld phase analysis of the XRD patterns had a significant effect on the calculated carbon weight percent content. These overshadowed the trends in the carbon content which prevented this approach from being used to calculate the true carbon mass in this work. For this reason, the “indicative carbon loss” calculation described above was used as an indicative measure of the true carbon loss.

### 3. Results and Discussion

#### 3.1 Powder Characterisation

The powder particles had a porous structure formed by the agglomeration of the dark contrast carbide grains and the bright contrast Ni alloy binder, Fig. 2. Both phases were of uniform contrast, indicating that they were of consistent composition and without significant concentration of sub-carbide phases. This was confirmed by XRD analysis which showed peaks from only  $\text{Cr}_3\text{C}_2$  (JCPDS 35-0804) and Ni (JCPDS 04-0850). The Ni peaks were shifted to lower  $2\theta$  positions due to alloying with Cr.

Table 2 contrasts the powder composition provided by the manufacturer with that measured by the techniques in this work as a benchmark for discussion on the coating compositions.



**Table 2 Amperit 588 powder characteristics**

Suppliers elemental composition		Rietveld XRD analysis
Elemental composition, wt. %		
Ni	19.4	14.6
Cr	70	74.1
C	10.6	11.2

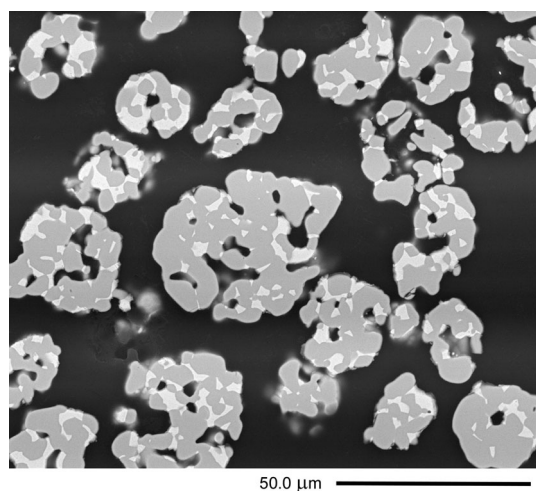
Suppliers elemental composition		EDS area analysis
Normalized Ni and Cr composition, wt. %		
Ni	21.7	22.4
Cr	78.3	77.6

Based on suppliers elemental composition	Image analysis	Rietveld XRD analysis
Carbide volume concentration, vol. %		
Carbide	79.5	87.4
Ni Alloy	20.5	12.6

Based on suppliers elemental composition	EDS spot scans	Rietveld XRD analysis
Ni alloy composition, wt. %		
Ni	86.6	92.05
Cr	13.5	7.95



**Fig. 2** Cross-sectional BSE image of the Amperit 588 powder

### 3.2 Coating Analysis

**3.2.1 Mach II Ar-H<sub>2</sub> Trials.** The Ar-H<sub>2</sub> plasma parameters settings with the Mach II anode nozzle were selected to use similar plasma gas compositions (H<sub>2</sub> flow was 9 vol.% in the “low flow” trial and 7.6 vol.% in the “high flow” trial) but at different total plasma gas flow rates, Table 1. The Mach II anode nozzle geometry is designed to generate high plasma plume velocities and so these trials were intended to explore the effect of plasma velocity for a comparable plasma composition, on the extent of carbide dissolution and carbon loss.

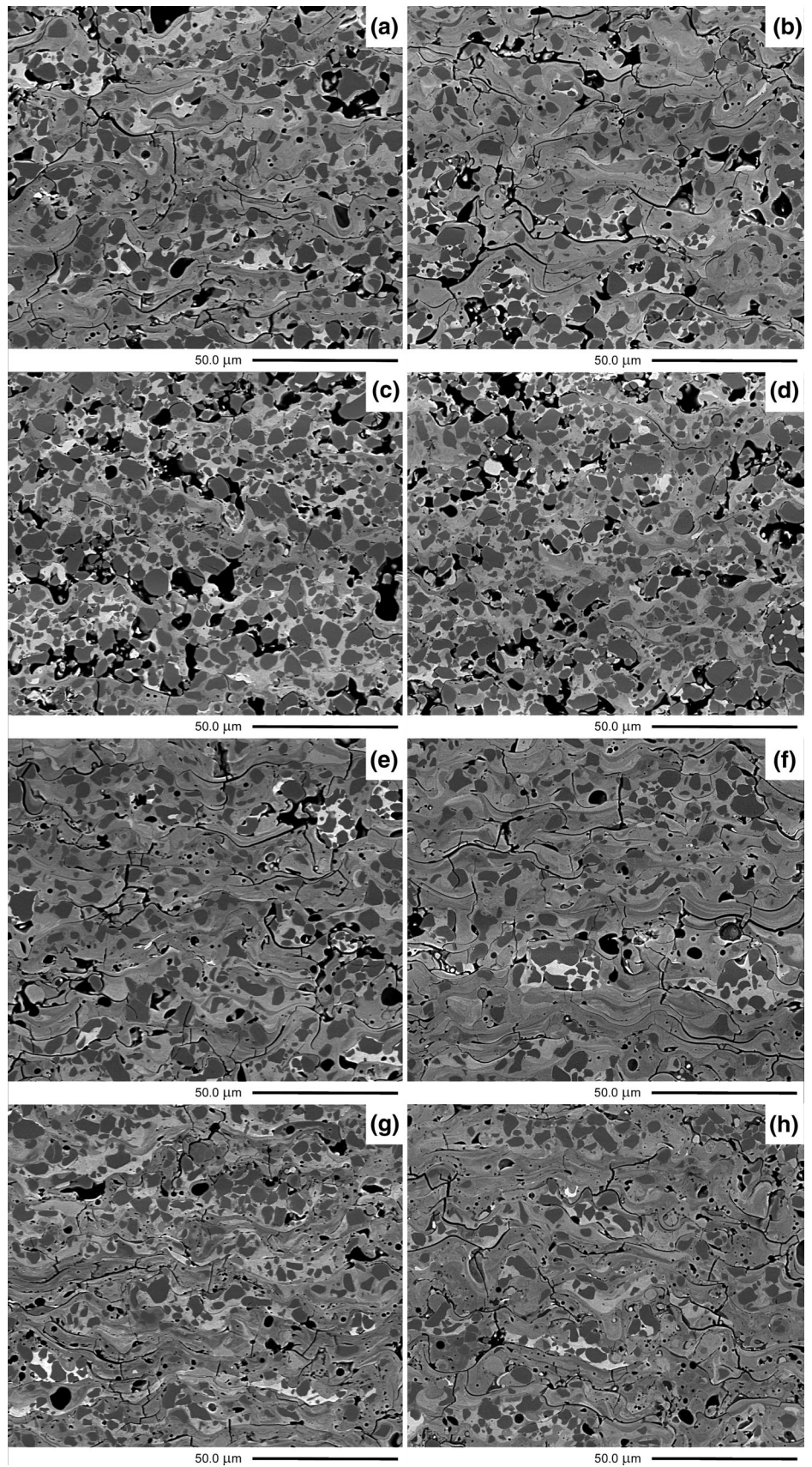
*Low Flow rate Trials: Unshrouded (Trials CD01 100 and 120 mm)* Figure 3 presents the BSE images of the coating cross section for the Mach II anode nozzle trials.

The darkest contrast features are porosity and low atomic mass oxides. The brightest contrast material is the high atomic mass Ni alloy binder, while the blocky dark gray features are the chromium carbides. The light gray zones of contrast between the Ni alloy and chromium carbides represent zones where the carbides dissolved into the Ni alloy to form material with a lower average atomic mass than that of the original Ni alloy. The majority of the large porosity features were generated by pullout of splat segments during metallographic preparation based on their angular morphology.

The unshrouded low flow Ar-H<sub>2</sub> plasma settings at 100 mm generated a dense coating microstructure in which the majority of splats were well molten and exhibited high degrees of carbide dissolution. However, there were notable numbers of partially molten particles evident by the bright contrast Ni-rich regions which retained high carbide contents. The coating was segregated by an extensive inter-splat and trans-splat crack network, similar to the crack networks seen in ceramic plasma spray coatings. It is postulated that dissolution of Cr and C from the dissolved carbide grains lead to embrittlement of the Ni alloy binder, making it prone to cracking under the tensile shrinkage stresses generated during solidification. In spite of the well-molten nature of the splats, oxide stringers were rarely observed. The high degree of carbide dissolution was reflected in the image analysis results which indicated a reduction in the carbide content from 79.5 vol.% in the powder to 27.8 vol.% in the coating, Fig. 4(a). Decarburisation of the molten particles lead to a reduction in the indicative carbon content of 10%, Fig. 4(b).

The coating XRD pattern showed a complex transition in composition from the starting powder, Fig. 5. The key features of this pattern were the formation of broad peaks

**Fig. 3** Cross-sectional BSE images of the unshrouded and shrouded coatings from the Mach II nozzle trials: CD01—100 mm (a) and 120 mm (b), CD02—100 mm (c) and 120 mm (d), CD03—100 mm (e) and 120 mm (f), CD04—100 mm (g) and 120 mm (h)



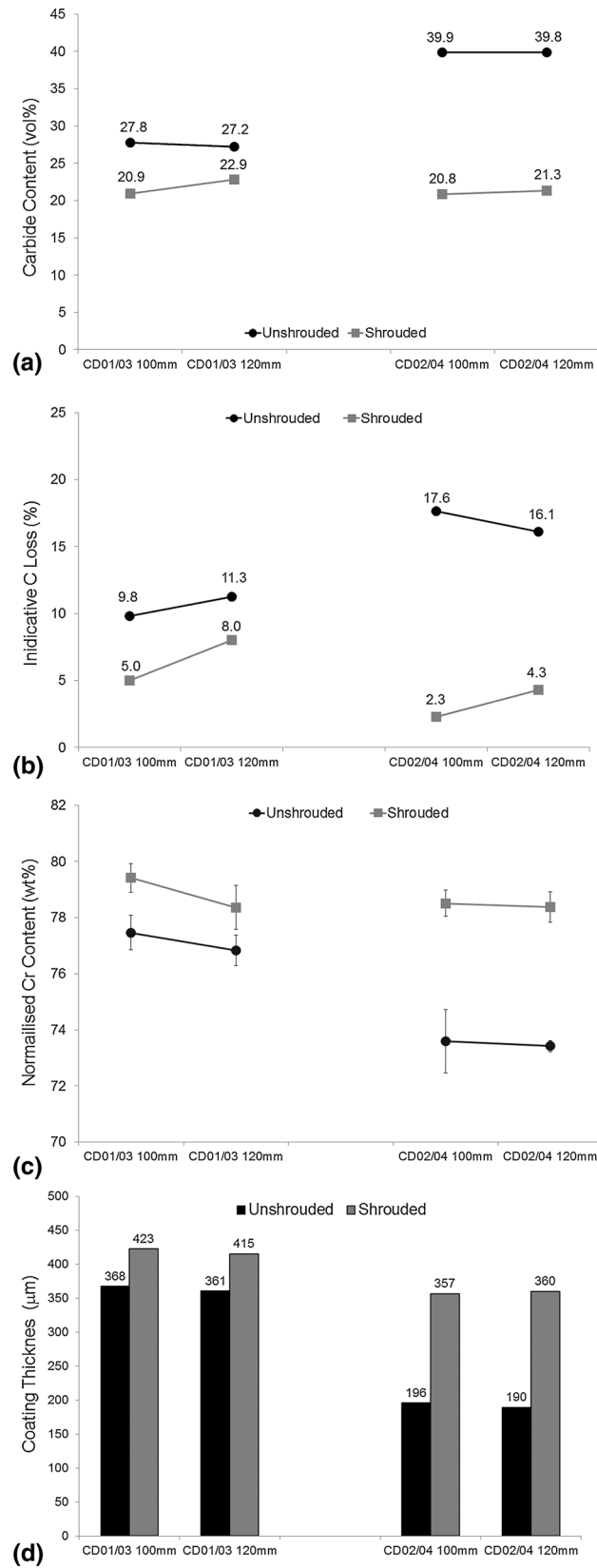


**Fig. 4** Analysis of the coating properties from the unshrouded and shrouded Mach II nozzle trials CD01-CD04 as a function of spray distance—carbide content (a), indicative carbon loss (b), normalized Cr content (c) and coating thickness (d)

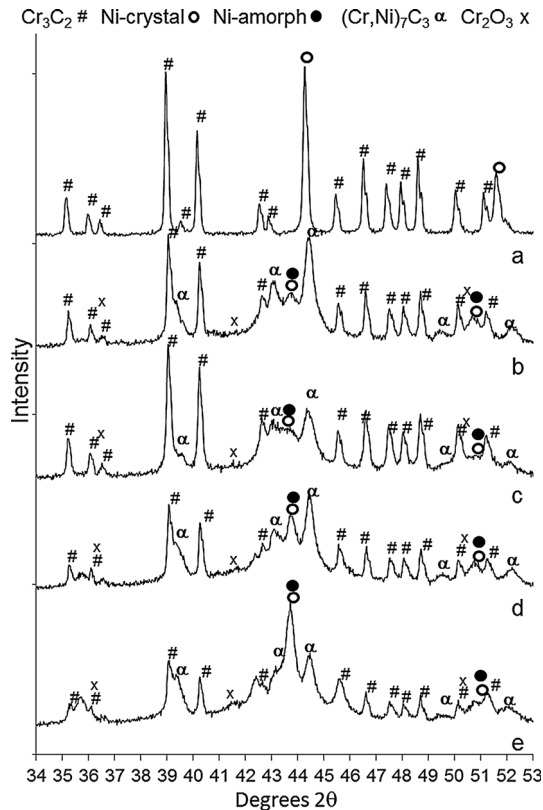


**Fig. 5** XRD patterns from the Amperit 588 powder (a), and trials CD01 (b), CD02 (c), CD03 (d), and CD04 (e) at 100 mm spray distance

in the regions  $2\theta = 42^\circ\text{--}45^\circ$  and  $50^\circ\text{--}53^\circ$ , in addition to the narrower crystalline  $\text{Cr}_3\text{C}_2$  peaks. The broad peaks are typically attributed to the formation of amorphous or nano-crystalline material generated by rapid solidification of the Ni alloy (Ref 5, 8, 16-23). The position of these peaks is typically shifted to lower  $2\theta$  positions relative to the Ni peaks in the starting powder due to increases in the Ni lattice parameter resulting from Cr and C dissolution (Ref 5, 8, 22, 23). Identification of carbides other than  $\text{Cr}_3\text{C}_2$  is complicated by the overlap of many of the peaks in the  $\text{Cr}_7\text{C}_3$  and  $\text{Cr}_{23}\text{C}_6$  XRD patterns with those of  $\text{Cr}_3\text{C}_2$  and the Ni alloy (Ref 6, 22). To overcome this limitation Rietveld analysis was used to fit reference patterns of the identified phases to the coating XRD patterns. A detailed analysis of this phase identification and the Rietveld quantification is presented in part 2 of this two-part article series (Ref 10). From this analysis four phases were assumed to be present—a crystalline  $\text{Cr}_3\text{C}_2$  phase, a crystalline Ni alloy phase, an amorphous/nano-crystalline Ni alloy phase, and a metastable  $(\text{Cr,Ni})_7\text{C}_3$  phase based on  $\text{Cr}_7\text{C}_3$ , Fig. 5. The reduction in the  $\text{Cr}_3\text{C}_2$  concentration, combined with the formation of large amounts of amorphous Ni and metastable  $\text{Cr}_7\text{C}_3$  material in the XRD pattern suggests that the carbide dissolved or melted into the molten Ni alloy in-flight. The low degree of carbon loss indicates that the dissolved Cr and C were largely retained within these phases. This is supported by the EDS area

analysis which showed an equivalent normalized Cr content in the coating to that in the starting powder, Fig. 4(c) (Cr content—77.6 vol.% in powder versus 77.5 vol.% in the coating).

The increase in spray distance from 100 to 120 mm had no significant visible effect on the cross-sectional coating microstructure, Fig. 3, and only a subtle effect on the carbide content, degree of carbon loss, retained Cr content, and the coating deposit efficiency based on the coating thickness, Fig. 4(a)-(d). The XRD pattern mirrored that at 100 mm, with the main variation being the more definitive, but still very low intensity, peaks of  $\text{Cr}_2\text{O}_3$ . The particles were obviously well molten at the point of impact, and therefore were capable of undergoing dynamic changes in composition and structure in response to variations in the plasma plume characteristics or simply as a function of the longer dwell time at the longer spray distance. The fact that such changes did not occur to an appreciable extent suggests that the particle velocity was high enough to prevent significant reaction of the particles with the environment (e.g. oxide formation or decarburisation) or to undergo significant internal phase transformations (e.g. carbide dissolution) over the extended spray distance.

*High Flow Rate Trials: Unshrouded (Trials CD02 100 and 120 mm)* In principle, the high flow rate Ar- $\text{H}_2$  plasma parameters of Trial CD02 were expected to generate higher particle velocities than in the previous low flow rate trials. The higher particle velocities would reduce the duration of the particle heating and the time of exposure to the gaseous environment, leading to reduced levels of carbide dissolution, decarburisation, and oxidation. These expectations were largely reflected in the microstructure of the coating sprayed at 100 mm under these conditions, Fig. 3. The coating contained significant pockets of porosity, both from pullout during metallographic preparation but also from inclusion of porous powder particles which had not melted fully prior to impact. Cracking was evident but mainly localized to inter-splat shrinkage cracks due to shrinkage upon solidification, rather than forming extensive crack networks. The carbide content was notably higher than in the low flow rate coating, Fig. 4(a), as were the regions of bright Ni-rich material, indicating a lower degree of carbide dissolution. However, the degree of indicative carbon loss was higher than in the low flow rate trials, Fig. 4(b). This apparently contradictory result was attributed to non-optimal powder injection conditions. The low viscosity of the Ar- $\text{H}_2$  plasma caused significant practical difficulties in tuning the carrier gas flow to achieve powder trajectories that would not impact the inner wall of the shroud in the subsequent shrouded trials. The very low carrier gas flows required to achieve this raised concerns about blocking of the powder feeder, the powder feed line or injector in the plasma torch, but none of these effects were observed during spraying. The low carrier gas flow meant that the powder did not effectively penetrate the plasma near the injection point, particularly in the high gas flow rate trial, but flowed along the periphery of the plasma plume. In this region, the powder would have seen lower plasma temperatures,

accounting for the reduced degrees of carbide dissolution, but would have been exposed to high oxygen concentrations from entrained air leading to higher levels of decarburisation. The reduced degree of carbide dissolution relative to the previous low flow rate trial was reflected in the XRD pattern which was dominated by  $\text{Cr}_3\text{C}_2$  peaks and the amorphous Ni alloy material, Fig. 5. The metastable  $\text{Cr}_7\text{C}_3$  peaks were of significantly lower relative intensity than in the previous trial and no  $\text{Cr}_2\text{O}_3$  peaks were observed. The EDS analysis indicated a reduction in the normalized Cr content relative to the powder (normalized Cr content in powder 77.6 versus 73.6 wt.% in the coating) but the cause of this was uncertain, Fig. 4(c). The deposition efficiency was significantly lower than in the low flow rate trial based on the coating thickness results, Fig. 4(d). While this was expected due to the higher particle velocities, and therefore lower degrees of particle heating, the result was compounded by the poor powder injection parameters which meant that a significant percentage of the powder was not heated sufficiently to form part of the coating.

The increase in spray distance from 100 to 120 mm had a minimal effect on the coating microstructure, Fig. 3, and the coating attributes assessed in this work, Fig. 4(a)-(d).

*Low Flow Rate Ar-H<sub>2</sub> Trials: Shrouded (CD03 100 and 120 mm)* Shrouding of the low flow rate Ar-H<sub>2</sub> plasma generated a greater degree of carbide dissolution relative to the unshrouded Trial CD01 at the 100 mm spray distance, Fig. 3. The concentration of bright contrast partially molten splats was notably lower, and the retained carbide grains were more isolated and of a lower concentration. This was reflected in the image analysis results which showed a reduction in the carbide content from 27.8 vol.% in the unshrouded trials to approximately 21% with shrouding, Fig. 4(a). In spite of the greater degree of carbide dissolution, the extent of decarburisation was dramatically reduced, with the magnitude of indicative carbon loss being half that of the unshrouded trial, Fig. 4(b). The metastable  $\text{Cr}_7\text{C}_3$  and amorphous Ni alloy phases became more dominant in the coating composition, with the  $\text{Cr}_3\text{C}_2$  peaks of lower relative intensity in the XRD pattern compared to the unshrouded trial, Fig. 5. The normalized Cr content was comparable with the starting powder, Fig. 4(c), indicating no preferential loss of this element with shrouding. The greater degree of particle heating with shrouding implied by the increase in carbide dissolution, lead to an increase in the deposit efficiency with the coating thickness increasing from 368 to 423  $\mu\text{m}$  with shrouding, Fig. 4(d).

The increase in spray distance from 100 to 120 mm had a minimal effect on the coating microstructure, Fig. 3, carbide content and coating thickness, Fig. 4(a) and (d). The main variation was in the degree of indicative carbon loss which increased from 5 to 8% in moving from 100 to 120 mm spray distance, Fig. 4(b). It is notable that while the magnitude of carbon loss is lower than in the unshrouded trial, the rate of carbon loss with spray distance is higher in the shrouded trial. The XRD patterns at both spray distances were comparable, and no oxide peaks were observed.

*High Flow Rate Ar-H<sub>2</sub> Trials: Shrouded (CD04 100 and 120 mm)* Shrouding dramatically increased the degree of carbide dissolution relative to the unshrouded trial under the high flow rate Ar-H<sub>2</sub> plasma parameters at the 100 mm spray distance. The coating microstructure was comparable with that produced under the previous shrouded low flow rate plasma conditions, showing the same high concentration of network cracking and extensive degree of carbide dissolution, Fig. 3. The splats were significantly thinner and more distorted than in the unshrouded coating, implying that they achieved higher temperatures and were more molten at impact. A notable feature was the presence of circular porosity features within the body of several well-molten splats. These were assumed to be gas bubbles formed by internal oxidation of carbon by dissolved oxygen to form  $\text{CO}/\text{CO}_2$  (Ref 24). While these circular porosity features were seen in the shrouded low flow rate coating (CD03) they appeared at a higher concentration in this coating. The similarity in the coating microstructures between this coating and the previous shrouded low flow rate plasma coating (CD03) was reflected in the comparable carbide content results based on image analysis, Fig. 4(a). This was in spite of the significantly higher plasma gas velocities, generated under these plasma conditions and the shorter time in-flight for carbide dissolution to occur. The most significant difference between the shrouded trials was in the extent of indicative carbon loss, with a notable reduction in the degree of decarburisation seen in the high flow rate trial in spite of the equivalent degree of carbide dissolution, Fig. 4(b). The fact that the degree of carbon loss was the lowest of all trials, while the particle velocity was the highest of all trials, indicates that the main mechanism of carbon loss was by in-flight decarburization and not bounce off of the carbide grains upon impact. There was also a notable difference in the XRD patterns between these coatings, particularly in the dominant metastable  $\text{Cr}_7\text{C}_3$  and Ni alloy peaks, suggesting some variation in how the dissolved carbide elements were retained in the coating, Fig. 5. The normalized Cr content in the shrouded coating was higher than in the unshrouded trial (CD02) and comparable with the starting powder, indicating that shrouding had prevented the mechanism of Cr loss from occurring, Fig. 4(c). The greater degree of particle heating with shrouding significantly improved the deposit efficiency with the coating thickness increasing from 196 to 357  $\mu\text{m}$  with shrouding, Fig. 4(d).

The increase in spray distance to 120 mm had only a minor effect on the coating microstructure, carbide content, and deposit efficiency, Fig. 3 and 4. The main variation was in the degree of indicative carbon loss which increased with increasing spray distance, Fig. 4(b).

*Effect of Shrouding* From the preliminary trials leading up to this work, it was noted that the solid conical coaxial shroud prevented air entrainment into the plasma over the first 90 mm of the spray distance (Ref 9). Because the plasma was not diluted with cold, slower moving air it was expected to retain a higher temperature and velocity over a significantly longer distance than in the unshrouded conditions (Ref 25-27). The particles were therefore ex-



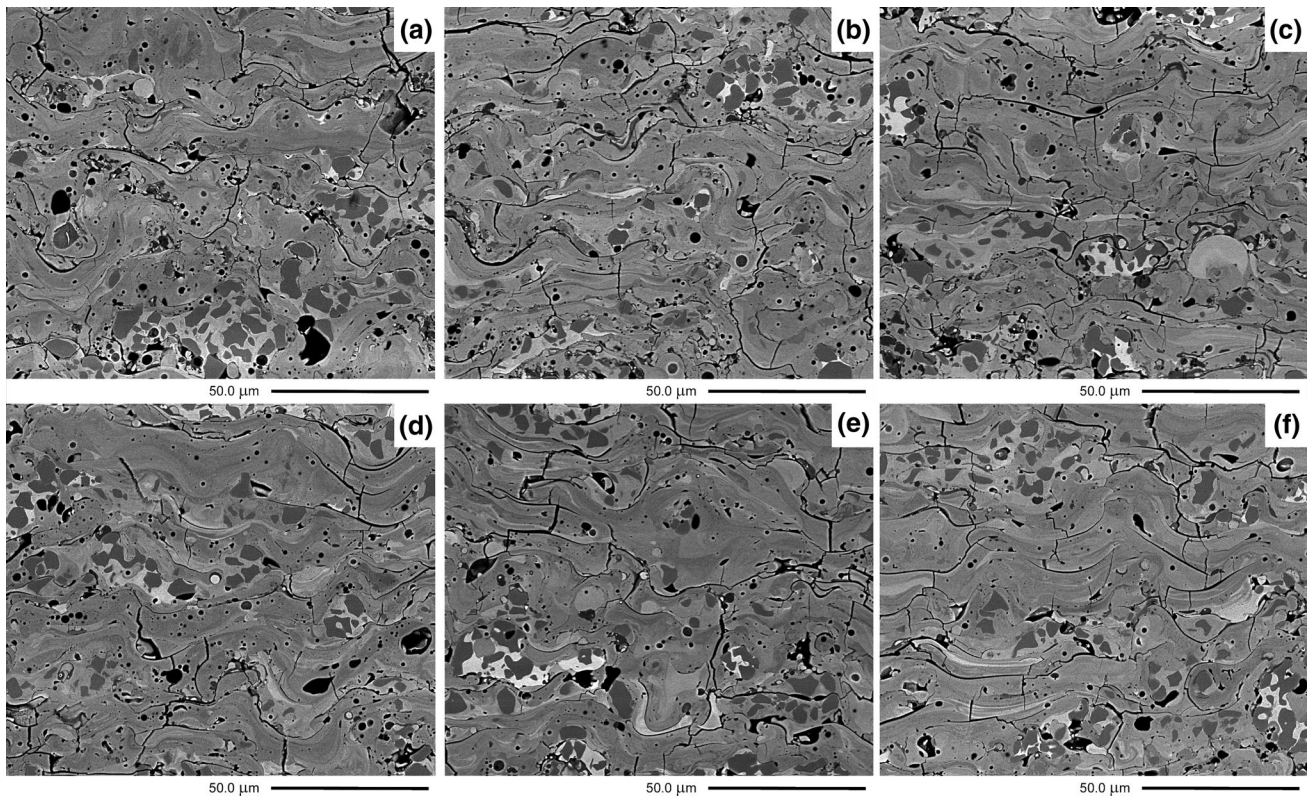


**Fig. 6** Cross-sectional BSE images of the coatings from trial CD05—80 mm (a), 100 mm (b), and 120 mm (c), and trial CD07—80 mm (d), 100 mm (e), and 120 mm (f)

pected to reach higher temperatures, and possibly higher velocities, while at the same time being exposed to very low oxygen concentrations over their time in-flight (Ref 26). The solid shroud also “contained” all of the powder particles injected into the plasma and directed them toward the substrate (Ref 9). This overcame the powder injection issues highlighted in the unshrouded trials and at the same time contributed to high deposit efficiencies. These benefits were evident at both 100 and 120 mm spray distances, with the shrouded coatings showing higher degrees of carbide dissolution, lower concentrations of partially molten splats, higher deposit efficiencies, and lower degrees of carbon loss.

While the extent of decarburisation was significantly reduced with shrouding, carbon loss did still occur in spite of the extreme measures taken to prevent oxygen ingress—specifically the use of a solid shield covering all but the last 10 mm (at the 100 mm spray distance) of the particle trajectory and the very high flow rate of external coaxial shroud gas which was expected to effectively seal off the plasma plume and sprayed particles from the surrounding air. As noted in the previous section, decarburisation under the conditions of this work occurs primarily through in-flight reaction of carbon dissolved in the molten Ni binder with oxygen to form CO/CO<sub>2</sub>. Carbon loss by carbide rebounding is assumed to be minimal, while carbon loss after impact is also assumed to be negligible for the reasons outlined in the review of decarburisation and because of the high flow of external argon

shroud gas. The requirement for oxygen exposure means that decarburisation must have occurred within the short exposure time between the particles exiting the shroud and impacting on the substrate. A similar situation occurred during the spraying of NiCr coatings with this shroud (Ref 12) and the mechanism postulated in that work is assumed to have occurred here. Because of the narrow internal shroud opening angle, the trajectory of the particles through the plasma leads to them passing near the inner wall at the bottom of the shroud near the shroud exit. When exiting the shroud this trajectory takes them into the path of the outer coaxial gas shroud. At short shroud-substrate separation distance, like those in this work, the gas shroud impinges on the substrate and generates a complex mixing zone in which ambient air is assumed to become entrained (Ref 27). The particles pass through this mixing zone prior to impact on the substrate. Extensive carbide dissolution into the Ni binder occurred prior to this point, leading to high concentrations of dissolved carbon. The molten particle temperature is also very high, favoring rapid diffusion, and reaction kinetics. Therefore, while the exposure time in this oxygen-enriched zone is short, the particles are in a physical state which makes them extremely susceptible to rapid decarburisation. While the “indicative carbon loss” results provide a single value for each coating, it is apparent that this is the summation from a broad distribution of extents of decarburisation as a function of powder particle size. The largest particles take longer to melt and undergo less

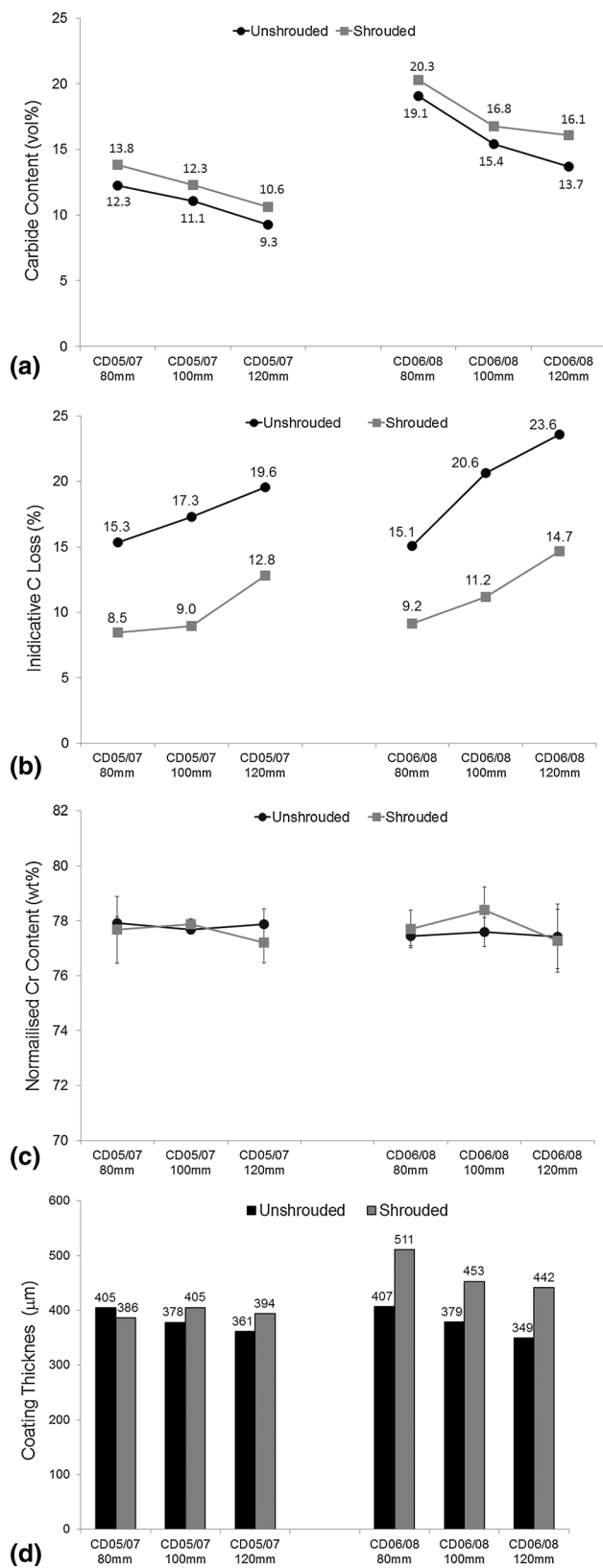


**Fig. 7** Analysis of the coating properties from the unshrouded and shrouded subsonic nozzle trials CD05-CD08 as a function of spray distance—carbide content (a), indicative carbon loss (b), normalized Cr content (c) and coating thickness (d)

carbide dissolution in-flight, making them less susceptible to decarburisation. In contrast, the smaller particles rapidly melt and dissolve all of their carbide grains soon after injection. Furthermore their high surface area to volume ratio means they are more susceptible to decarburisation than larger particles, meaning that they are likely to play a dominant role in the overall degree of carbon loss. This particle-size distribution effect is compounded further in this trial due to the non-optimal injection conditions. This meant that the smaller particles tended to follow along the periphery of the plasma plume near the shroud wall, making them particularly susceptible to becoming caught up in the turbulent oxygen-enriched mixing zone upon exiting the shroud.

The increase in spray distance from 100 to 120 mm is short, but occurs over the region where dramatic changes in the plasma temperature, velocity, and composition take place (Ref 25, 27). The close proximity of the substrate, combined with the increased separation of the shroud from the substrate leads to complex mixing of the plasma plume, the shroud gas, and entrained air (Ref 12). This complex mixed zone is expected to be larger and more developed in the 120 mm trials compared to at 100 mm. As such, the plasma temperature and velocity that the molten particles experience changes dramatically over this distance. The effect of these changes on the particle temperature and velocity is expected to be dependent upon the particle size distribution—smaller particles responding rapidly to these changes while larger particles responding more sluggishly. In the unshrouded trials, there is also a region of rapid change in the plasma temperature and velocity in the near-substrate region. However, the change in plasma conditions that the particle experience is expected to be less dramatic and occur over a longer time because air entrainment into the plasma occurs early and over a long period of spray distance and there is no high flow of cold shrouding gas. These changes in the plasma plume characteristics with and without shrouding directly influence the particle temperature and velocity profiles, which in turn determine the extent of carbide dissolution, carbon loss, and the deposit efficiency. In contrasting the results in this section, it appears that the degree of carbide dissolution and deposit efficiency are most closely linked to the particle temperature, while the degree of indicative carbon loss is more closely linked to the oxygen content in the gas environment. The higher deposit efficiency and lower retained carbide content in the shrouded trials indicate that the particles reached higher temperatures. However, in considering the effect of spray distance, there is very little change in carbide content with increasing distance across all trials. In the coating thickness results, there is a general decrease in thickness with increasing distance, but this change is small and the magnitude of the change is relatively consistent between the unshrouded and shrouded trials for each plasma setting. These results imply that the physical state of the particles that formed the coating did not change significantly over the 100 to 120 mm distance in either the unshrouded or shrouded trials. This result is attributed to the high particle velocities generated using

the Mach II nozzle under both the high flow rate and low flow rate plasma conditions.

In considering the degree of indicative carbon loss, the response with increasing spray distance was expected to be more significant in the shrouded trials. In the unshrouded trials, the particles are exposed to oxygen over a longer duration of the spray distance and hence the rate of change in carbon content between 100 and 120 mm was expected to be less significant than in the shrouded trials in which the particles have only just been exposed to an oxygen containing atmosphere. This effect is thought to contribute to the higher rate of change in the indicative carbon loss for the shrouded trial versus the unshrouded trial under the low flow rate Ar-H<sub>2</sub> settings (A similar comparison could not be made for the high flow rate settings as the non-optimal powder injection conditions are believed to have had a significant complicating effect on the trial results).

In contrasting the results of the shrouded trials alone, the magnitude of carbon loss and the rate of change of carbon loss with spray distance were both lower for the high gas flow rate plasma settings. This was also attributed to the higher particle velocities generated under these conditions and therefore the shorter exposure time over which decarburisation could occur. A contributing factor may have been the higher volume of plasma gas in the plasma plume which would have more effectively displaced the shroud gas and any entrained air away from the trajectory of the in-flight particles, further minimizing their exposure to oxygen and decarburisation.

**3.2.2 Subsonic Trials.** The “subsonic” anode nozzle geometry was expected to generate plasma plume characteristics more comparable with those of “standard” plasma systems presented in the literature, compared to the Mach II anode nozzle. In particular, the plasma velocity was expected to be notably lower. This in turn would generate lower particle velocities, which would increase the particle residence time in the plasma, leading to higher temperatures and the potential for greater degrees of carbide dissolution, oxidation, and decarburisation to occur. The Ar-He and Ar-H<sub>2</sub> plasma parameter settings used were found to generate the greatest degrees of carbide dissolution in preliminary trials (Ref 9) and enabled the effect of the plasma composition to be contrasted. The shrouded trials were performed with a coaxial gas shroud in contrast to the solid conical coaxial shroud used in the Mach II anode nozzle trials.

*Ar-He Low Flow Rate Trials: Unshrouded (CD05 80, 100 and 120 mm)* The unshrouded low flow Ar-He plasma parameter settings at 80 mm generated dramatically greater degrees of carbide dissolution than seen in any of the unshrouded Mach II anode nozzle trials, Fig. 6. The dense coating structure was segregated by an extensive crack network and contained high concentrations of the circular porosity features noted in the previous coatings. Oxide features were present as isolated oxide stringers and as particulate agglomerates indicative of oxide dust inclusions. The majority of splats showed total carbide dissolution, with carbide grains retained only in isolated

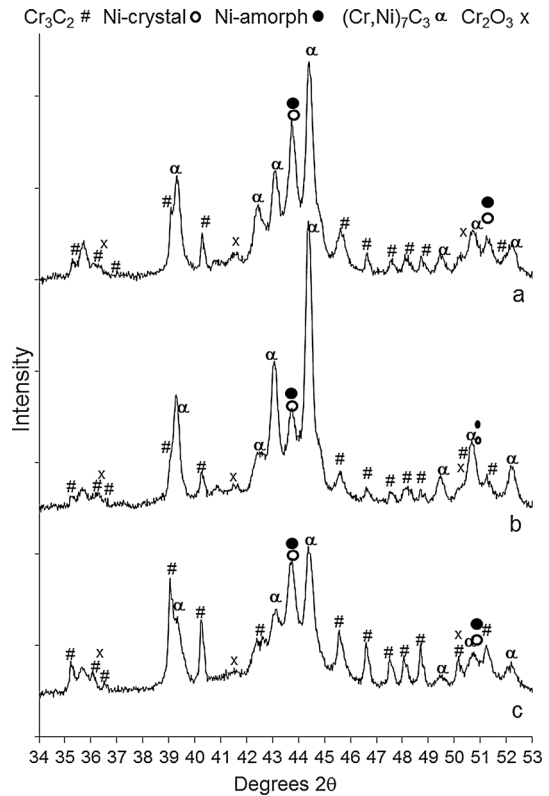
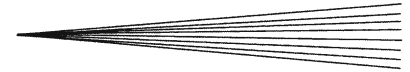


**Fig. 8** XRD patterns from trial CD05 at 80 mm (a) and 120 mm (b), and CD07 at 80 mm (c)

partially molten splats. This was reflected in the low carbide content results of 12.3 vol.%, less than half that is seen in the unshrouded Mach II trials, Fig. 7(a). However, the increased degree of carbide dissolution leads to a greater degree of decarburisation, with an indicative carbon loss of 15%, Fig. 7(b). The coating composition was dominated by the metastable Cr<sub>7</sub>C<sub>3</sub> phase and to a lesser extent the amorphous Ni alloy, Fig. 8. Peaks from Cr<sub>3</sub>C<sub>2</sub> were still present but at significantly lower relative intensities than seen in the Mach II trials. Cr<sub>2</sub>O<sub>3</sub> peaks were clearly identified and of a higher relative intensity than in the previous trials. The normalized Cr content was comparable with that of the starting powder, indicating no preferential loss of this element. The coating thickness was 405 μm, which was only slightly higher than that seen in the unshrouded low flow rate Mach II anode nozzle trials.

The increase in spray distance to 100 and 120 mm leads to only subtle visible changes in the coatings microstructure, Fig. 6. Oxide features, particularly as dust inclusions, increased in concentration with increasing distance. The number of carbide rich, partially molten splats decreased in concentration with increasing spray distance. This was reflected in the image analysis quantification of the carbide content which showed a linear decrease in carbide concentration down to 9 vol.% at 120 mm, Fig. 7(a). Conversely, the degree of indicative carbon loss showed a linearly increasing trend with spray distance, reaching al-



most 20% at 120 mm, Fig. 7(b). With the increase in carbide dissolution with spray distance, the coating composition became increasingly dominated by the metastable  $\text{Cr}_7\text{C}_3$  phase, while the relative intensity of the  $\text{Cr}_3\text{C}_2$  peaks gradually decreased.  $\text{Cr}_2\text{O}_3$  remained the only oxide phase observed in all trials, but the relative intensity of this phase did not vary significantly with spray distance. EDS analysis indicated no change in the normalized Cr content with spray distance, Fig. 7(c). The deposit efficiency decreased with increasing spray distance, with the coating thickness decreasing in a linear manner from 405  $\mu\text{m}$  at 80 mm to 361  $\mu\text{m}$  at 120 mm, Fig. 7(d).

The BSE images in Fig. 6 indicated that the majority of the impacting particles had undergone total carbide dissolution at distances shorter than 80 mm. The changes in carbide content, therefore, must reflect the slower degree of carbide dissolution in largest particles which were included as partially molten splats at 80 mm and underwent progressively greater degrees of carbide dissolution with increasing spray distance. The smaller particles rapidly melted soon after injection enabling carbide dissolution into the melt to occur at short distances downstream. The particle temperature most likely continued to increase to exceed the melting point of  $\text{Cr}_3\text{C}_2$  [ $T_{\text{MELT}\text{Cr}_3\text{C}_2} = 1813^\circ\text{C}$  (Ref 28)] based on the extreme degrees of carbide dissolution evident at 80 mm. With increasing particle size, the particle would take longer to heat up and melt the Ni binder, thereby delaying the start of carbide dissolution to further downstream and significantly reducing the time over which dissolution could occur. Furthermore, the particle temperature is not expected to reach the levels of the smaller particles and evidently did not reach the melting temperature of  $\text{Cr}_3\text{C}_2$  based on the presence of retained carbide grains in the coating. The lower temperature would also reduce the kinetics of carbide dissolution.

The fact that the degree of carbide dissolution in the large partially molten splats increased with spray distance implies that the Ni binder in these particles remained molten out to 120 mm. The reduction in deposit efficiency, is therefore is unlikely to be due to bounce off of large particles that did not receive sufficient heating to melt and adhere to the coating. Instead it is postulated that the reduced deposit efficiency resulted from the smaller particles cooling, and potentially solidifying, prior to impact and so bouncing off the substrate or being swept away from the surface by the impacting gas stream. Vaporization could, in principle, also play a role although this is considered unlikely over the 80-120 mm distance as the plasma plume is expected to be cooling to well below the boiling temperature of the powder components in this range due to air entrainment.

*Ar-He Low Flow Trial: Shrouded (CD07 80, 100 and 120 mm)* Gas shrouding had no significant effect on the microstructure in the BSE images of the coatings sprayed at 80 mm, Fig. 6. The circular porosity features seen in the unshrouded coating and attributed to internal CO formation were also seen in this coating in high concentrations. This was surprising in that the argon gas shrouding was expected to protect the particles from oxidation, or at

least dilute the oxygen concentration to levels where significant internal dissolution of oxygen into the molten binder was minimized. The presence of these bubbles therefore indicates that either the gas shroud was ineffective in preventing oxygen penetration to the particles, or that an alternative mechanism of bubble formation occurs e.g. inclusion of air pockets from within the porous powder particles due to rapid melting of the particle periphery, or dissolution of plasma gases within the molten binder at high temperature. The results of this work do not definitively support either of these scenarios—carbon loss decreased with shrouding, indicating it did prevent oxygen ingress, while trapping of gas bubbles from the porous powder or dissolution of plasma gases would be expected to generate more widespread bubble formation across all the coatings which was not observed. The majority of splats again showed total carbide dissolution, with  $\text{Cr}_3\text{C}_2$  grains limited to the isolated partially molten splats. Image analysis indicated that the carbide content was higher in the shrouded coating than in the unshrouded trial, Fig. 7(a). This indicated a lower degree of carbide dissolution with shrouding, the opposite effect to that observed in the Mach II anode nozzle trials with the solid conical coaxial shroud. The degree of indicative carbon loss was significantly lower than in the shrouded trial at 8.5%, Fig. 7(b). The lower amount of carbon loss is contributed to the beneficial effect of the gas shroud reducing the extent of decarburisation, but also the lower degree of carbide dissolution. The latter implies that lower particle temperatures were achieved, along with less carbon dissolved into the Ni binder, both of which would contribute to reducing the extent of decarburisation. The XRD pattern showed the same phases as in the unshrouded trial, but the reduced degree of carbide dissolution meant that the  $\text{Cr}_3\text{C}_2$  peaks were of higher relative intensity and the metastable  $\text{Cr}_7\text{C}_3$  peaks did not dominate the pattern to the same extent, Fig. 8. No change in the normalized Cr content occurred with shrouding, which was consistent with the lack of Cr variation in the unshrouded trial, Fig. 7(c). In contrast to the general trends observed in the Mach II anode nozzle trials, shrouding generated no improvement in the deposit efficiency with the coating thickness lower than in the unshrouded trial, Fig. 7(d).

With increasing spray distance to 100 and 120 mm the coating microstructure showed the same subtle transitions as in the unshrouded trial, with a gradual increase in the extent of carbide dissolution in the partially molten splats, Fig. 6. The carbide content linearly decreased with increasing spray distance at the same rate as in the unshrouded trial, Fig. 7(a). The degree of indicative carbon loss showed a more complex trend with increasing spray distance, Fig. 7(b). Over the 80-100 mm distance the degree of carbon loss increased only a minor amount, but the rate of carbon loss from 100 to 120 mm was significantly higher. This was in contrast to the linear increase in carbon loss seen in the unshrouded trial over this spray distance. The XRD coating composition showed the same transitions in phase concentration as noted in the unshrouded trial. However, in marked contrast to the unshrouded trials,  $\text{Cr}_2\text{O}_3$  peaks were not observed in the 80

and 100 mm trials. No significant change in the normalized Cr content occurred with shrouding out to 120 mm, Fig. 7(c). The coating thickness remained consistent with increasing spray distance and did not decrease in the manner seen in the unshrouded trial, Fig. 7(d).

**Effect of Shrouding** In contrast to the solid coaxial conical shroud trials, gas shrouding in the Ar-He subsonic anode nozzle trials generated no improvement in the degree of carbide dissolution or the deposit efficiency relative to the unshrouded trials. However, it was effective in reducing the degree of carbon loss. Kim (Ref 29) reported similar observations during gas shrouded Ar-H<sub>2</sub> plasma spraying of tungsten powders using a similar shroud design. These observations are a direct result of the variations in shroud design. The solid conical coaxial shroud physically prevented air entrainment over the majority of the spray distance. The lack of dilution with cold, slow moving air meant that the plasma maintained higher temperatures and velocities relative to the unshrouded case. This generated greater heating of the particles, leading to more extensive carbide dissolution and higher deposit efficiencies, while minimizing oxygen exposure and decarburisation. In contrast the gas shroud design relied primarily on the coaxial cylindrical gas curtain formed around the plasma to protect the particles in-flight. The lack of a physical barrier between the gas shroud and the plasma meant that the shroud gas became entrained within the plasma in the same way that air was entrained in the plasma in the unshrouded case (Ref 29). Entrainment of the colder shroud gas cools and potentially slows the plasma plume, meaning that the shroud provides minimal benefits in extending the high temperature, high-velocity region of the plasma. As a result, the particle temperature and velocity profiles between 80 and 120 mm are not expected to vary significantly between the unshrouded and shrouded trials. This would account for the consistent carbide dissolution and deposit efficiency results with and without shrouding. The magnitude of the gas shroud entrainment effect on cooling and slowing of the plasma may actually be higher than in the case of the unshrouded trial due to the continual high flow rate of cold shroud gas into the region around the plasma versus entrainment of still ambient air in the unshrouded case (Ref 30-32).

In the same way that the shroud gas becomes entrained within the plasma plume through eddy formation and turbulent mixing, the shroud gas entrains the surrounding ambient air. Eventually this entrained air is mixed within the plasma itself, exposing the spray particles to oxygen and subsequent decarburisation. In this way the practical effectiveness of gas shrouding lies in shielding the plasma plume initially and delaying the point at which entrained oxygen meets the plasma centreline, until further downstream than in the unshrouded case. Beyond this point the shroud gas serves to flood the plume with argon, effectively diluting the oxygen concentration of the gas surrounding the particles. In comparison with the unshrouded case, decarburisation is delayed until further downstream, after which the rate of decarburisation is potentially reduced due to the lower oxygen concentration.

A contributing factor to the significance of the above effects is the trajectory of the particles and their relationship to the three dimensional temperature and velocity profiles of the plasma (Ref 33), and the zones of shroud gas and ambient air entrainment. Initially, the trajectory of the particles passes through the plasma plume region, where the particles undergo the greatest degree of heating and acceleration, Fig. 9. While significant carbide dissolution occurs in this zone, the oxygen content is low and so negligible decarburisation occurs. The particle trajectory gradually passes through the plasma centreline and the particles exit the bottom of the plasma plume. At this point, shroud gas has become entrained within the plasma and reached the centreline of the spray axis. The particles are exposed to a generally cooling and decelerating gas plume in this region, but the oxygen concentration is still low so decarburisation remains limited. Over the last zone of the spray distance, the particles pass through a complex mixed gas zone in which significant air entrainment has occurred. Furthermore, the trajectory of the particles takes them further away from the plasma centreline and in to regions of ever increasing oxygen content. Decarburisation in this zone is expected to occur at an increasing rate, particularly as the majority of particles will have undergone significant, if not total, carbide dissolution by this time. This mechanism is postulated to contribute to the trend in indicative carbon loss with spray distance for the gas shrouded Ar-He trials (Note a similar trend was also observed in the following Ar-H<sub>2</sub> trial). A low degree of decarburisation was observed over the 80-100 mm spray distance, before showing a significant increase in the amount of carbon loss from 100 to 120 mm. At these long distances, the particle trajectory is farthest from the plasma centreline and increasingly exposed to increasing oxygen concentrations, potentially accounting for the indicated transition in the rate of decarburisation.

**Ar-H<sub>2</sub> Low Flow Rate Trials: Unshrouded (Trial CD006 80, 100 and 120 mm)** The use of hydrogen instead of helium as the secondary gas generates significant changes in the plasma characteristics, and therefore, in the particle temperature and velocity profiles as highlighted in

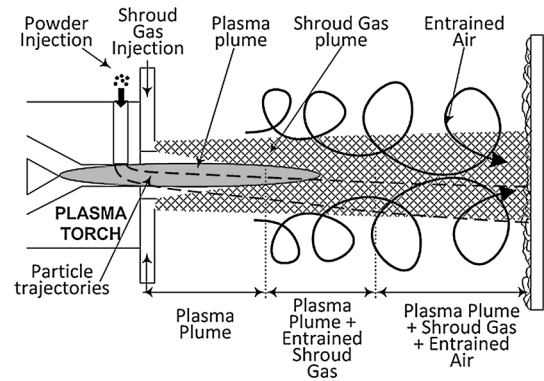


**Fig. 9** Schematic diagram illustrating the trajectory of particles through the plasma plume, the plasma+entrained shroud gas region, and finally the plasma plume+shroud gas+entrained air region prior to impact

the initial trials (Ref 9). In general, Ar-H<sub>2</sub> plasmas have lower viscosities compared to Ar-He plasmas (Ref 34). This results in lower particle velocities and therefore longer exposure times in the hot zone of the plasma. The lower viscosity also results in greater air entrainment into the plasma (Ref 35, 36). Furthermore, the use of hydrogen instead of helium increases the plasma thermal conductivity (Ref 34, 37), generating more effective heating of the particles and higher average particle temperatures. In principle, therefore, the longer residence times and higher average temperatures in the Ar-H<sub>2</sub> plasma would favor higher degrees of carbide dissolution. However, the higher oxygen content in the plasma due to air entrainment would mean greater degrees of decarburisation under these conditions. However, it must be noted that these generalized effects are dependent upon the specific plasma parameters used (gas flow rate and current) and critically upon the powder injection conditions and resulting particle trajectories through the plasma. While these factors form the basis of qualitative comparison between the Ar-He and Ar-H<sub>2</sub> plasma results in the following sections, no quantitative comparisons can be made because the specific particle velocities and temperatures were not measured in each trial.

The coating sprayed at 80 mm under the low flow rate Ar-H<sub>2</sub> plasma parameters had a dense structure with a similar extensive crack network as seen in the previous Ar-He coating at this distance, Fig. 10. A notable

difference was the significantly lower concentration of round porosity features attributed to internal CO formation within the well-molten splats. Dark contrast oxides were present primarily as oxide stringers between the splats. The majority of splats showed total carbide dissolution, however, the carbide content appeared higher than in the Ar-He coating. The carbides were present as large rounded grains within partially molten splats that had not deformed to the same extent as the highly molten, high carbide dissolution splats. The carbide content image analysis results reflected this observation with the carbide content of 19% greatly exceeding that of the Ar-He coating, Fig. 7(a). In spite of the lower degree of carbide dissolution the extent of indicative carbon loss was comparable to that seen in the Ar-He coating, Fig. 7(b). This result implies that under the powder injection conditions used in this work, air entrainment and the resulting decarburization of the particles was significantly higher in the Ar-H<sub>2</sub> plasma at 80 mm than in the Ar-He plasma. This is postulated to result from the lower density of the Ar-H<sub>2</sub> plasma (Ref 34) which resulted in air entrainment occurring at shorter distances than in the higher density Ar-He plasma (Ref 35). Accentuating this effect was the fact that the lower plasma density meant that the particle trajectories passed through the plasma and out into the “plasma + entrained air” mixed zone at shorter distances than in the Ar-He trials, based on how far the particles deviated from the plasma centreline when impacting the

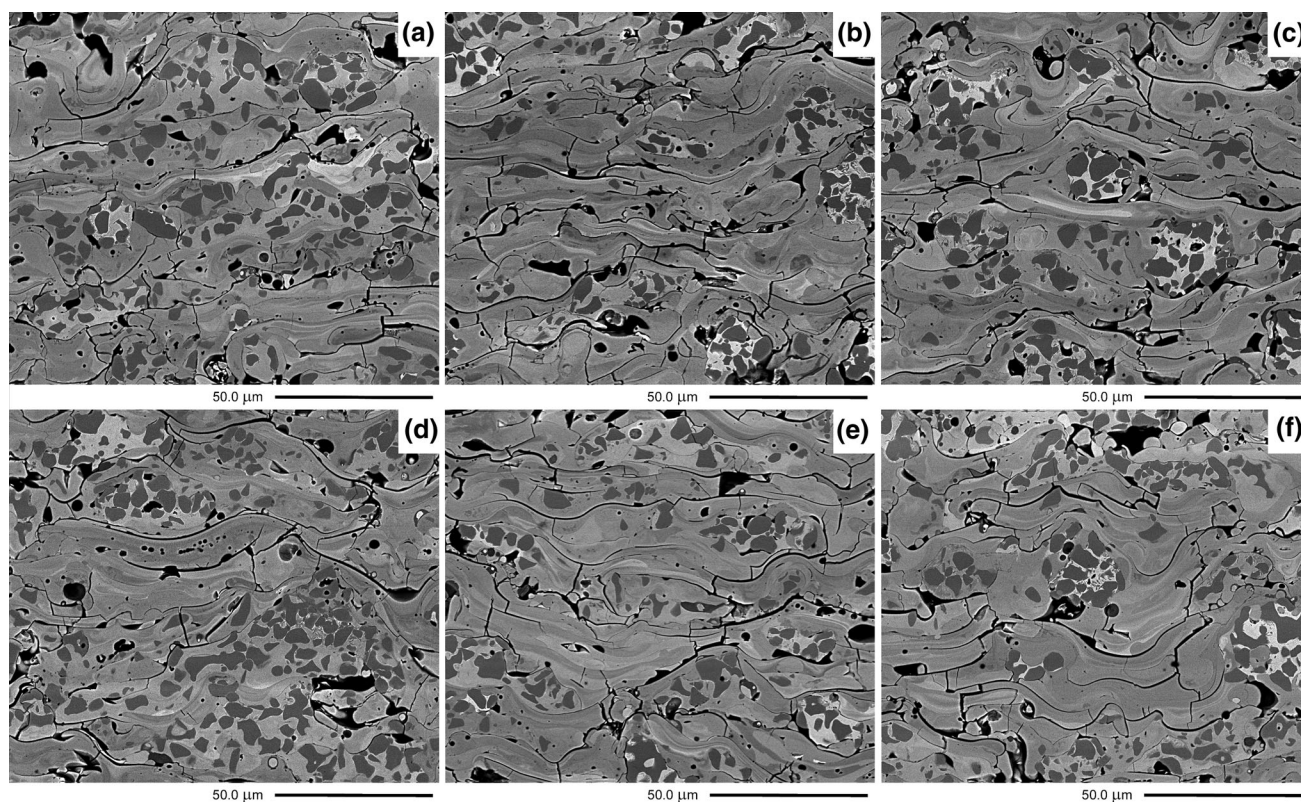


**Fig. 10** Cross-sectional BSE images of the coatings from trial CD06—80 mm (a), 100 mm (b), and 120 mm (c), and trial CD08—80 mm (d), 100 mm (e), and 120 mm (f)

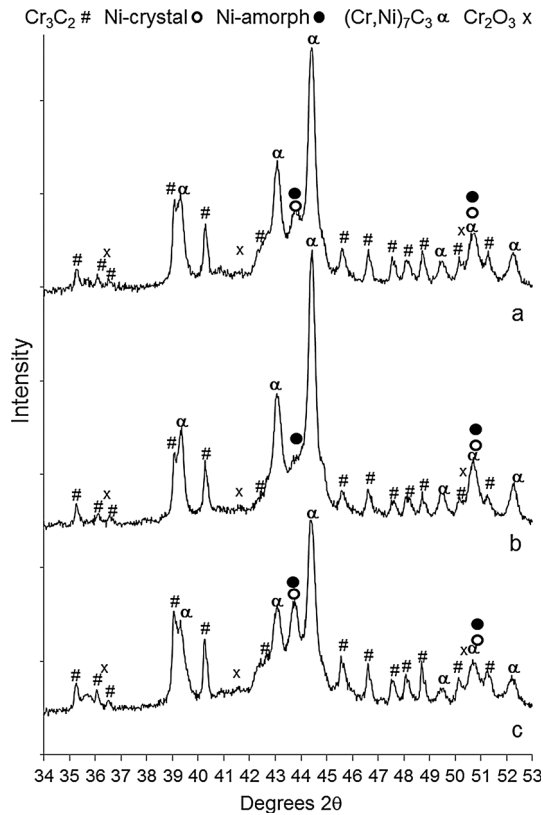


**Fig. 11** XRD patterns from trial CD06 at 80 mm (a) and 120 mm (b), and CD08 at 80 mm (c)

substrate. As a result, the particles would have been exposed to higher oxygen concentrations over a longer time period. Since carbide dissolution is assumed to have occurred soon after injection into the plasma, the extended oxygen exposure would have accentuated the degree of carbon loss via CO formation. The XRD pattern was dominated by the metastable  $\text{Cr}_7\text{C}_3$  phase, with the  $\text{Cr}_3\text{C}_2$  peaks of low relative intensity, Fig. 11(a). No  $\text{Cr}_2\text{O}_3$  peaks were observed in the XRD pattern. The normalized Cr content was comparable to that in the starting powder, indicating no preferential loss of this element, Fig. 7(c). In spite of the lower degree of carbide dissolution, and therefore the implied reduction in degree of particle heating, the coating deposit efficiency was the same as in the previous Ar-He plasma sprayed coating at 80 mm, Fig. 7(d).

The increase in spray distance to 100 and 120 mm resulted in only a slight reduction in the number of high carbide content, partially molten splats, Fig. 10, which was reflected in the carbide content results, Fig. 7(a). Given the high degree of carbide dissolution in the smaller particles evident at 80 mm, these changes in carbide content reflect the increase in dissolution of carbide grains within the larger partially molten particles in the same way as noted in the Ar-He coating. The magnitude of carbide dissolution, however, was distinctly lower than that seen in the Ar-He trial at each spray distance. The degree of carbon loss due to decarburisation increased with

increasing spray distance, with the 23.6% loss at 120 mm the highest recorded value across all trials, Fig. 7(b). The rate of carbon loss with increasing spray distance was higher than that in the Ar-He trial. This supports the comments above regarding the greater extent of oxygen exposure of the particles in the Ar- $\text{H}_2$  plasma due to greater air entrainment and the variation in particle trajectory. The coating composition became increasingly dominated by the metastable  $\text{Cr}_7\text{C}_3$  phase with increasing spray distance at the expense of both the  $\text{Cr}_3\text{C}_2$  and Ni alloy phase peaks, Fig. 11(b).  $\text{Cr}_2\text{O}_3$  peaks appeared as indicative features at 100 mm and were more definitive but still of low intensity in the 120 mm coating. The extended exposure in the plasma with spray distance did not lead to any preferential loss of Cr from the coating, Fig. 7(c). The coating deposit efficiency showed a linear decreasing trend with increasing spray distance, with the coating thickness reducing from 407  $\mu\text{m}$  at 80 mm to 349  $\mu\text{m}$  at 120 mm. This reduction was assumed to result from the same mechanism as highlighted in the Ar-He trial. However, in contrasting the results of this trial with the Ar-He trial, it can be seen that there is a more significant change in deposit efficiency as a function of spray distance under the Ar- $\text{H}_2$  parameters, Fig. 7(d). This effect relates in some way to the variation in the plasma plume temperature and velocity profiles with spray distance for the two plasma compositions as well as the variation in plasma density and its effect on the particle velocity and trajectories.

*Ar- $\text{H}_2$  Low Flow Rate Trial: Shrouded (CD08 80, 100 and 120 mm)* Gas shrouding had a minimal effect on the coating appearance, Fig. 10, or carbide content at 80 mm, Fig. 7(a). These results imply that gas shrouding had a negligible effect, or even slightly negative effect, on the powder temperature profile in-flight, and hence on the carbide dissolution, in the same way as noted in the Ar-He trial. Gas shrouding was, however, effective in reducing the extent of carbon loss at 80 mm from 15 to 9% with shrouding, Fig. 7(b). Since the degree of carbide dissolution was comparable in both the unshrouded and shrouded coatings, this reduction in carbon loss is a direct measure of the effectiveness of the shroud in reducing oxygen penetration into the plasma. The changes in coating composition mirrored those seen in the unshrouded trial, Fig. 11(c), with again no evidence of  $\text{Cr}_2\text{O}_3$  formation or changes in the normalized Cr content, Fig. 7(c). The most significant effect of shrouding was in the deposit efficiency, which resulted in an increase in coating thickness from 407 to 511  $\mu\text{m}$ . This is in direct contrast to the results of the Ar-He trial and the mechanism accounting for this effect is not immediately apparent. In the solid shroud trials, the increase in deposit efficiency was attributed to the greater degree of heating of the particles, as implied by the increase in carbide dissolution and the confinement of the powder stream by the shroud, which directed the powder particles toward the substrate. In this case, the gas shroud did not influence the degree of carbide dissolution and is assumed to have had a negligible effect on the particle temperature and hence also on the deposit efficiency. Instead, it is postulated that the high gas flow rate of the cold

shroud gas created a gas “tunnel” effect that constrained the plasma and particle stream within the plasma (Ref 25). This channeled the particles in the direction of the substrate rather than allowing them to penetrate through the plasma and into the surrounding air where they could be carried away in the periphery of the plasma plume. At longer distances the shroud gas becomes well entrained in the plasma plume, but the higher mass flux that this creates relative to entrainment of air would also be expected to assist in directing the particles toward the substrate. The higher deposit efficiency would result simply from more of the particles impacting and adhering to the surface, rather than an increase in their average temperature. The reason why this effect was not observed in the Ar-He plasma may be related to the differences in density between these two plasma compositions and therefore the effectiveness of the shroud in “containing” the denser Ar-He plasma, and the powder injection parameters used in each trial.

The coating microstructure exhibited the same subtle variations with increasing spray distance as noted in the unshrouded trial, Fig. 10. The carbide content decreased with increasing spray distance in approximately the same manner as seen in the unshrouded trial, Fig. 7(a). The degree of carbon loss increased with spray distance but was significantly lower than the unshrouded trial at each spray distance, Fig. 7(b). There is the suggestion of a transition in the rate of carbon loss from 80 to 100 mm and 100 to 120 mm, but this is less definitive than in the Ar-He trial and requires additional testing to confirm the effect. However, the overall rate of carbon loss with distance was lower than in the unshrouded trial, indicating that the effect of gas shrouding extended out to 120 mm. The XRD-based coating phase distribution developed in the same manner as in the unshrouded coating with increasing spray distance, with the main variation being in the lack of oxide formation out to 120 mm. Similarly, no significant changes in the normalized Cr content occurred with shrouding, Fig. 7(c). The deposit efficiency was consistently higher than in the unshrouded trials at each distance out to 120 mm, but the rate of reduction was comparable to that of the unshrouded trials (coating thickness variation of 58  $\mu\text{m}$  in the unshrouded trial and 70  $\mu\text{m}$  in the shrouded trial over the 80-120 mm range), Fig. 7(d).

**3.2.3 Relationship between Carbide Content and Carbon Loss.** Decarburisation of  $\text{Cr}_3\text{C}_2\text{-NiCr}$  particles during thermal spraying occurs by dissolution of the carbide elements into the molten Ni binder, followed by diffusion of carbon to the surface where it reacts with oxygen to form gaseous CO. The magnitude of carbon loss should therefore be proportional to the extent of carbon dissolution. Figure 12 plots the indicative carbon loss as a function of the carbide content measured by image analysis for all of the samples in this work. The results show that, across all trials, the coating carbide content, and therefore the degree of carbide dissolution, is not a direct measure of carbon loss. The degree of carbon loss is also dependent upon the spray conditions, particularly the concentration of oxygen that the particles are exposed to. However, for a given spray system the results indicate that

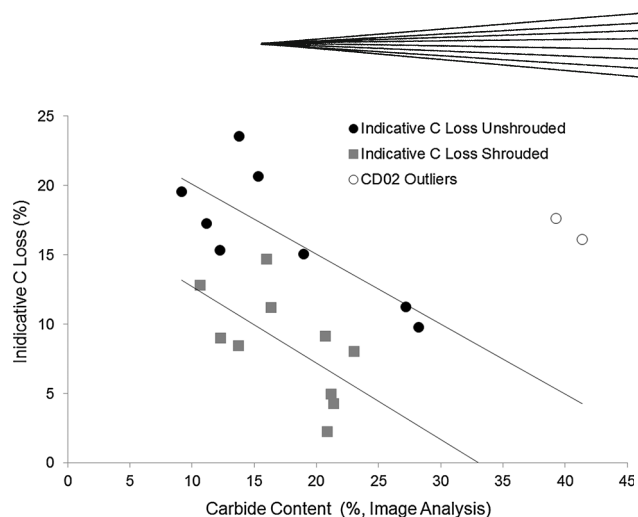


**Fig. 12** Variation in the indicative carbon loss as a function of the coating carbide content for the unshrouded and shrouded trials

lower retained carbide concentrations, i.e. higher degrees of carbide dissolution, result in higher degrees of carbon loss. This is illustrated by the linear lines of best fit through the unshrouded and shrouded results in Fig. 12. The data from Trial CD02 were excluded from the line of best fit fitting as they were considered outliers generated by the poor powder injection parameters.

## 4. Conclusions

The aim of Part 1 of this two-part article series was to characterize the effect of spray distance on the extent of carbide dissolution and carbon loss during high energy plasma spraying of  $\text{Cr}_3\text{C}_2\text{-NiCr}$  coatings. Trials were sprayed using “subsonic” and high-velocity “Mach II” anode nozzle plasma configurations, over the spray distance 80-120 mm and 100-120 mm, respectively. Two shroud configurations were investigated and the results contrasted with unshrouded trials. The main conclusions from this work were:

- The high-velocity Mach II anode nozzle trials were sprayed using an Ar- $\text{H}_2$  plasma under low and high flow rate settings. In the unshrouded low flow rate trials, the increase in spray distance from 100 to 120 mm had only a minor effect on the degree of carbide dissolution, carbon loss, and deposit efficiency due to the high particle velocity. Shrouding significantly increased the extent of carbide dissolution and the deposit efficiency, while reducing the degree of carbon loss relative to the unshrouded trial. The high particle velocity again resulted in no significant changes in the coating attributes with spray distance, aside from the degree of indicative carbon loss which increased with spray distance.
- The unshrouded high flow rate Mach II anode nozzle trials were significantly influenced by non-optimal powder injection conditions which resulted in lower carbide dissolution but higher carbon loss relative to



the lower flow rate trials. Shrouding overcame these poor injection issues by enclosing all of the injected powder within the plasma plume. This dramatically increased the degree of carbide dissolution and the deposit efficiency, while reducing the degree of indicative carbon loss. The increase in spray distance had a minor effect on the main coating attributes but did lead to an increase in the degree of carbon loss. The increase in carbon loss with spray distance in the shrouded trials was attributed to the particles passing through a complex gas mixing zone outside the shroud where they were exposed to entrained air prior to impact.

- The lower velocity subsonic anode nozzle trials were sprayed using Ar-He and Ar-H<sub>2</sub> plasmas. In the unshrouded Ar-He trials, increasing spray distance lead to a reduction in the coating carbide content and deposit efficiency, but an increase in the degree of indicative carbon loss. Shrouding dramatically reduced the magnitude of carbon loss, but the degree of carbon loss still increased with increasing spray distance. There was a notable transition in the rate of carbon loss beyond 100 mm which was attributed to the combined effect of the particle trajectory moving away from the protective gas shroud and increased turbulent mixing and ambient air entrainment at longer distances. In contrast to the Mach II trials, shrouding did not lead to an increase in carbide dissolution, which was attributed to cooling of the plasma by entrainment of the cold shroud gas. In the Ar-H<sub>2</sub> trials, the same trends in coating attributes with spray distance with and without shrouding were observed as in the Ar-He trials. The main variation was that the rate of change in the coating properties was notably higher in the Ar-H<sub>2</sub> trials. This was attributed to the variation in particle temperature and velocity between the two plasmas as a result of the different plasma thermal conductivity and density generated with the different secondary gases.
- The coating carbide content was found to be a poor generic indicator of the extent of carbon loss. However, for a given spray system, lower coating carbide contents (i.e. higher degrees of carbide dissolution) resulted in higher degrees of carbon loss.

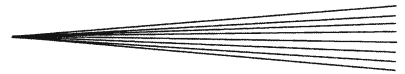
## Acknowledgments

The author gratefully acknowledges the support of Associate Professor Brian Gabbitas and the University of Waikato for their collaboration in the development and manufacture of the shrouds and for allowing their use in this work. The assistance of Holster Engineering in performing the spray trials is sincerely appreciated. The support in the preparation and analysis of the coatings provided by the Department of Chemical and Materials Engineering at the University of Auckland is also gratefully appreciated. Funding for this work was provided by

the Marsden Fund Council from New Zealand Government funding, administered by the Royal Society of New Zealand.

## References

1. I. Fagoaga, J.L. Viviente, P. Gavin, J.M. Bronte, J. Garcia, and J.A. Tagle, Multilayer Coatings by Continuous Detonation System Spray Technique, *Thin Solid Films*, 1998, **317**, p 259-265
2. J. He, M. Ice, and E. Lavernia, Synthesis of Nanostructured Cr<sub>3</sub>C<sub>2</sub>-25(Ni20Cr) Coatings, *Metall. Mater. Trans. A*, 2000, **31A**, p 555-564
3. D. Poirier, J.-G. Legoux, and R. Lima, Engineering HVOF-Sprayed Cr<sub>3</sub>C<sub>2</sub>-NiCr Coatings: The Effect of Particle Morphology and Spraying Parameters on the Microstructure, Properties and High Temperature Wear Performance, *J. Therm. Spray Technol.*, 2013, **22**(2-3), p 280-289
4. S. Matthews, B. James, and M. Hyland, The Role of Microstructure in the High Velocity Erosion of Cr<sub>3</sub>C<sub>2</sub>-NiCr Thermal Spray Coatings: Part 1—As-Sprayed Coatings, *Surf. Coat. Technol.*, 2009, **203**, p 1086-1093
5. F. Otsubo, H. Era, T. Uchida, and K. Kishitake, Properties of Cr<sub>3</sub>C<sub>2</sub>-NiCr Cermet Coating Sprayed by High Power Plasma and High Velocity Oxy-Fuel Processes, *J. Therm. Spray Technol.*, 2000, **9**(4), p 499-504
6. S. Zimmermann and H. Kreye, Chromium Carbide Coatings Produced with Various HVOF Spray Systems, *Thermal Spray: Practical Solutions for Engineering Problems*, C.C. Berndt, Ed., ASM International, Materials Park, 1996, p. 147-152
7. S. Matthews, "Erosion-Corrosion of Cr<sub>3</sub>C<sub>2</sub>-NiCr High Velocity Thermal Spray Coatings," Ph.D. Thesis, Department of Chemical and Materials Engineering, The University of Auckland, 2004
8. S. Matthews, M. Hyland, and B. James, Long-Term Carbide Development in High Velocity Oxygen Fuel/High Velocity Air Fuel Cr<sub>3</sub>C<sub>2</sub>-NiCr Coatings Heat Treated at 900°C, *J. Therm. Spray Technol.*, 2004, **13**(4), p 526-536
9. S. Matthews, Development of High Carbide Dissolution/Low Carbon Loss Cr<sub>3</sub>C<sub>2</sub>-NiCr Coatings by Shrouded Plasma Spraying, *Surf. Coat. Technol.*, 2014, **258**, p 886-900
10. S. Matthews, Compositional Development as a Function of Spray Distance in Unshrouded/Shrouded Plasma Sprayed Cr<sub>3</sub>C<sub>2</sub>-NiCr Coatings, *J. Therm. Spray Technol.*, 2014. doi:10.1007/s11666-014-0212-0
11. M. Jankovic, J. Mostaghimi, and V. Pershin, Design of a New Nozzle for Direct Current Plasma Guns with Improved Spraying Parameters, *J. Therm. Spray Technol.*, 2000, **9**(1), p 114-120
12. S. Matthews, Shrouded Plasma Spray of Ni-20Cr Coatings Utilizing Internal Shroud Film Cooling, *Surf. Coat. Technol.*, 2014, **249**, p 56-74
13. W.S. Rasband, ImageJ, US National Institute of Health, p. <http://imagej.nih.gov/ij/>, 1997-2012
14. L. Lutterotti, Total Pattern Fitting for the Combined Size-Stress-Texture Determination in Thin Film Diffraction, *Nucl. Inst Methods Phys. Res.*, 2010, **B**(268), p 334-340
15. J.K. Chen, D. Farkas, and W.T. Reynolds, Jr., Atomistic Simulation of an f.c.c/b.c.c Interface in Ni-Cr Alloys, *Acta Mater.*, 1997, **45**(11), p 4415-4421
16. J.M. Guilemany, J. Nutting, and N. Llorca-Isern, Microstructural Examination of HVOF Chromium Carbide Coatings for High-Temperature Applications, *J. Therm. Spray Technol.*, 1996, **5**(4), p 483-489
17. J. He and E.J. Lavernia, Precipitation Phenomenon in Nanostructured Cr<sub>3</sub>C<sub>2</sub>-NiCr Coatings, *Mater. Sci. Eng. A*, 2001, **301**(1), p 69-79
18. G.C. Ji, C.J. Li, Y.Y. Wang, and W.Y. Li, Microstructural Characterization and Abrasive Wear Performance of HVOF Sprayed Cr<sub>3</sub>C<sub>2</sub>-NiCr Coating, *Surf. Coat. Technol.*, 2006, **200**(24), p 6749-6757
19. M. Magnani, P.H. Suegama, N. Espallargas, C.S. Fugivara, S. Dosta, J.M. Guilemany, and A.V. Benedetti, Corrosion and Wear



- Studies of  $\text{Cr}_3\text{C}_2\text{-NiCr}$ -HVOF Coatings Sprayed on AA7050 T7 Under Cooling, *J. Therm. Spray Technol.*, 2009, **18**(3), p 353-363
20. J.K.N. Murthy, S. Bysakh, K. Gopinath, and B. Venkataraman, Microstructure Dependent Erosion in  $\text{Cr}_3\text{C}_2\text{-20(NiCr)}$  Coating Deposited by a Detonation Gun, *Surf. Coat. Technol.*, 2007, **202**(1), p 1-12
  21. J.K.N. Murthy, K. Satya Prasad, K. Gopinath, and B. Venkataraman, Characterisation of HVOF Sprayed  $\text{Cr}_3\text{C}_2\text{-50(Ni20Cr)}$  Coating and the Influence of Binder Properties on Solid Particle Erosion Behaviour, *Surf. Coat. Technol.*, 2010, **204**(24), p 3975-3985
  22. M.H. Staia, M. Suárez, D. Chicot, J. Lesage, A. Iost, and E.S. Puchi-Cabrera,  $\text{Cr}_3\text{C}_2\text{-NiCr}$  VPS Thermal Spray Coatings as Candidate for Chromium Replacement, *Surf. Coat. Technol.*, 2013, **220**, p 225-231
  23. T. Tomita, Y. Takatani, K. Tani, and Y. Harada, Mechanisms of High Hardness in  $\text{Cr}_3\text{C}_2\text{-NiCr}$  Cermet Coatings Formed by Vacuum Plasma Spraying, *Proceedings of the International Thermal Spray Conference*, 2001, p. 699-704
  24. K. Korpiola, "High temperature oxidation of metal, alloy and cermet powders in HVOF spraying process," Ph.D. Thesis, Department of Materials Science and Rock Engineering, Helsinki University of Technology, 2004
  25. D.T. Gawne, T. Zhang, and B. Liu, Computational Analysis of the Influence of a Substrate, Solid Shield and Gas Shroud on the Flow Field of a Plasma Jet, *Surf. Coat. Technol.*, 2002, **153**, p 138-147
  26. M.P. Planche, H. Liao, and C. Coddet, Oxidation Control in Atmospheric Plasma Spraying Coating, *Surf. Coat. Technol.*, 2007, **202**, p 69-76
  27. H. Wang, X. Chen, and W. Pan, Effects of the Length of a Cylindrical Solid Shield on the Entrainment of Ambient Air into Turbulent and Laminar Impinging Argon Plasma Jets, *Plasma Chem. Plasma Process.*, 2008, **28**, p 85-105
  28. M. Venkataraman and J.P. Neumann, The C-Cr (Carbon-Chromium) System, *Bull. Alloy Phase Diagr.*, 1990, **11**(2), p 152-159
  29. S. Kim, S. Choi, G.-H. Kim, and S.H. Hong, Effects of Shroud Gas Injection on Material Properties of Tungsten Layers Coated by Plasma Spraying, *Thin Solid Films*, 2010, **518**, p 6369-6372
  30. R.H. Henne, J. Arnold, G. Schiller, and T. Kavka, Improvement of DC Thermal Plasma Spraying by Reducing the Cold Gas Entrainment Effect, *Proceedings of the 2005 International Thermal Spray Conference: Thermal Spray Connects: Explore its Surfacing Potential*, E. Lugscheider, Ed., DVS-Verlag GmbH, Germany, 2005, p. 615-621
  31. K.D. Kang and S.H. Hong, Numerical Analysis of Shroud Gas Effects on Air Entrainment into Thermal Plasma Jet in Ambient Atmosphere of Normal Pressure, *J. Appl. Phys.*, 1999, **85**(9), p 6373-6380
  32. M.F. Morks and C.C. Berndt, Corrosion and Oxidation Properties of NiCr Coatings Sprayed in Presence of Gas Shroud System, *Appl. Surf. Sci.*, 2010, **256**, p 4322-4327
  33. W.D. Swank, J.R. Fincke, and D.C. Haggard, Plasma/Particle Interaction in Subsonic Argon/Helium Thermal Plasma Jets, *Thermal Spray Coatings: Research, Design and Applications—Proceedings of the 1993 National Thermal Spray Conference*, C.C. Berndt and T.F. Bernecki, Ed., ASM International, Materials Park, 1993, p. 25-30
  34. M. Boulos, P. Fauchais, and E. Pfender, *Thermal Plasmas—Fundamentals and Applications*, Plenum, New York, 1994
  35. A. Denoirjean, O. Lagnoux, P. Fauchais, and V. Sember, Oxidation Control in Atmospheric Plasma Spraying: Comparison Between Ar/H<sub>2</sub>/He and Ar/H<sub>2</sub> Mixtures, *Proceedings of the 15th International Thermal Spray Conference*, 1998, p. 809-814
  36. G. Di Girolamo, F. Marra, L. Piloni, G. Pulci, J. Tirillò, and T. Valente, Microstructure and Wear Behavior of Plasma-Sprayed Nanostructured WC-Co Coatings, *Int. J. Appl. Ceram. Technol.*, 2013, **10**(1), p 60-71
  37. A.A. Syed, A. Denoirjean, P. Fauchais, and J.C. Labbe, On the Oxidation of Stainless Steel Particles in the Plasma Jet, *Surf. Coat. Technol.*, 2006, **200**, p 4368-4382